Pre-print Statement for

"Fe_5S_2 identified as a host for sulfur in Earth and planetary cores"

Claire C. Zurkowski[a †], Barbara Lavina[b,c], Abigail Case[a], Kellie Swadba[a], Stella Chariton[b], Vitali B. Prakapenka[b], Andrew J. Campbell[a]

[a]The University of Chicago, Department of the Geophysical Sciences, 5734 S Ellis Ave, Chicago, IL 60637, USA
[b]Center for Advanced Radiation Sources, The University of Chicago, 9700 South Cass Avenue, Lemont, IL 60439, USA
[c]X-ray Science Division, Advanced Photon Source, Argonne National Laboratory, Lemont, IL 60439, USA
[†]Now at Earth and Planets Laboratory, Carnegie Institution for Science, 5251 Broad Branch Road, NW, Washington, DC 20015, USA

Corresponding Author: Claire Zurkowski, czurkowski@carnegiescience.edu

Dear Earth Arxiv,

This manuscript is a non-peer reviewed preprint submitted to *EarthArXiv*. It has been submitted for peer review at *Earth and Planetary Science Letters.*

Sincerely,
Claire Zurkowski

Fe_5S_2 identified as a host of sulfur in Earth and planetary cores

Claire C. Zurkowski[a †], Barbara Lavina[b,c], Abigail Case[a], Kellie Swadba[a], Stella Chariton[b], Vitali Prakapenka[b], Andrew J. Campbell[a]

[a]University of Chicago, Department of the Geophysical Sciences, 5734 S Ellis Ave, Chicago, IL 60637, USA
[b]Center for Advanced Radiation Sources, 9700 South Cass Avenue, Building 434A, Argonne, IL 60439, USA
[c]X-ray Science Division, Advanced Photon Source, Argonne National Laboratory, Argonne, IL 60439, USA
[†]Now at Earth and Planets Laboratory, Carnegie Institution for Science, 5251 Broad Branch Road, NW, Washington, DC 20015, USA

Corresponding Author: Claire Zurkowski, czurkowski@carnegiescience.edu

ABSTRACT

Cosmochemical considerations suggest that sulfur is a light alloying element in rocky planetary cores of varying sizes and oxidation states. High pressure-temperature (*P*-*T*) iron-sulfide phase relations therefore play a role in inner core crystallization and outer core thermochemical convection in a wide range of planetary bodies. The iron-saturated Fe-S phase relations were investigated to 200 GPa and 3250 K using single-crystal and powder X-ray diffraction techniques in a laser-heated diamond anvil cell. At high temperatures between 120 and 200 GPa, a hexagonal sulfide was synthesized with recrystallized hcp-Fe. The unit-cell parameters and diffraction intensities reveal an Fe_5S_2 stoichiometry adopting the Ni_5As_2 structure ($P6_3cm$, $Z = 6$). Fe_5S_2 is characterized by significant Fe-Fe bonding, complex coordination environments, and positional disorder and polytypism along the *c*-axis. Upon heating at 120 GPa, *I*-4 Fe_3S is observed to break down into Fe_5S_2 + Fe, whereas with heating above 120 GPa, Fe_2S + Fe reacts to form Fe_5S_2 + Fe at high temperatures. A *C*23–*C*37 Fe_2S transition is observed above 130 GPa. These results establish that Fe_5S_2 is the stable Fe-rich sulfide across much of Earth's outer core and will crystallize over an extensive depth up to the core-mantle boundary as the core

cools overtime. The increased metal-metal bonding observed in Fe_5S_2 compared to the other high *P-T* iron sulfides would likely contribute to signatures of higher conductivity from regions of Fe_5S_2 crystallization. As Earth's core is multicomponent, Fe_5S_2 could further serve as a host for Ni and Si as has been observed in the related meteoritic phase perryite, $(Fe, Ni)_8(P, Si)_3$, adding intricacies to elemental partitioning during inner core crystallization. The stability of Fe_5S_2 presented here is key to understanding the role of sulfur in the crystallization sequences that drive the geodynamics and dictate the structures of Earth and rocky planetary cores.

1. INTRODUCTION

Earth and the terrestrial planets are composed of silicate mantles and iron-rich metallic cores (e.g. Birch 1952; Mcdonough and Sun 1995). Earth's core is comprised of a convecting liquid metal outer core and an actively crystallizing, denser inner core (Birch 1952; Dziewonski and Anderson 1981; Fearn and Loper, 1981). The seismically determined 3-8% density deficit in Earth's core compared to pure iron is thought to be accounted for by cosmochemically abundant light alloying elements, such as Si, O, S, C, and H (Masters and Gubbins, 2003; Irving et al. 2018; Kuwayami et al. 2020; McDonough 2003), that introduce complex *P-T*-dependent melting and crystallization thermodynamics and help drive core convection as planets cool over time (Fearn and Loper, 1981; Stevenson 1981; 1988; Nimmo 2015).

While there remains no method to directly sample Earth's or any terrestrial planetary core, iron meteorites are recognized as core relics of disrupted planetesimals, and have long provided insight into the light elements that sequester into the metallic component of planetary interiors (e.g. Scott and Wasson 1975; Malvin et al. 1984). Of the candidate core-alloying elements, sulfur is present in nearly all iron meteorites, suggesting that sulfur is a core alloying

element in rocky planets of varying sizes, oxidation states, and formation histories (Scott and Wasson 1975; Jones and Drake, 1983; Kruijer et al. 2014). Sulfur easily alloys with iron to high pressures and temperatures, it is depleted in the silicate mantle compared to chondrites, and it lowers the melting temperature of pure iron (e.g. Evans 1970; Fei 1995; McDonough and Sun 1995; Fei et al. 1997; Ozawa et al. 2013; Tateno et al. 2019). It follows that during the high energy impact conditions of late stage proto-Earth formation, sulfur would have facilitated metal melt formation and density driven core segregation (Ringwood 1966; Murthy and Hall 1970; Shannon and Agee, 1996; Stevenson, 1988; Yoshino et al., 2003). Examination of the structural properties of iron sulfides at high *P*-*T* is therefore fundamental to characterizing the chemistry and thermodynamics of Earth and planetary cores.

The Fe-S phase relations are sensitive to *P*-*T*-composition conditions, and numerous Fe-rich sulfide compounds have been observed: FeS, Fe_3S_2, Fe_2S, and Fe_3S (Evans 1970; King and Prewitt 1982; Fei et al. 1995; Fei et al. 1997; Fei et al. 2000; Koch-Müller et al. 2002; Kamada et al. 2010; Ozawa et al. 2013; Mori et al. 2017; Tateno et al. 2019). Fe_3S is reported to be the stable Fe-rich sulfide between 21 and 250 GPa (Fei et al. 2000; Kamada et al. 2010; Ozawa et al. 2013), making it relevant at Earth's outer core conditions. Single crystal analysis of recovered Fe_3S from 21 GPa establishes that it adopts a Fe_3P-type structure (*I*-4, *Z*=8) (Fei et al. 2000), and no structural transitions have been reported in Fe_3S to 250 GPa (Ozawa et al. 2013; Kamada et al. 2010; Thompson et al. 2020; Seagle et al. 2006; Morard et al. 2008; Mori et al. 2017). Above ~250 GPa, Fe_3S breaks down at low temperatures into a *B*2 FeS + Fe phase assemblage, and FeS+Fe reacts at high temperatures to form *C*37 Fe_2S + Fe at 306 GPa (Ozawa et al. 2013; Mori et al. 2017; Tateno et al. 2019).

Although tetragonal Fe_3S has been reported to be stable to pressures encompassing Earth's upper-to-mid-outer core, crystal structure analysis of Fe_3S has not been conducted at Earth's core pressures, and unit-cell parameters for Fe_3S have only been reported up to 120 GPa at high temperatures (Seagle et al. 2006; Morard et al. 2008; Thompson et al. 2020). In the current study, Fe-rich Fe-S compositions were probed using single crystal and powder X-ray diffraction techniques which revealed that at high-temperatures between 120–200 GPa, hcp-Fe coexists with a hexagonal Fe_5S_2 sulfide (Ni_5As_2-type, $P6_3cm$, $Z = 6$). This complex crystal structure exhibits pervasive positional disorder and various stacking variations, such that single-crystal diffraction techniques were critical in identifying its crystal-chemistry. Increasing across the pressure range of 120–200 GPa, we find that Fe_3P-type Fe_3S + Fe, *C*23 Fe_2S + Fe , and *C*37 Fe_2S + Fe all react at high temperatures to form Fe_5S_2 + hcp-Fe. The single-crystal derived structures for *C*23 Fe_2S, *I*-4 Fe_3S, and *C*37 Fe_2S are also presented. The stability of Fe_5S_2 with recrystallized iron to 200 GPa at high temperatures reveals that Fe_5S_2 will eventually crystallize over a significant depth range of Earth's outer core.

2. MATERIALS AND METHODS

Experiments targeting multigrain synthesis in the Fe-S system consisted of mixtures of Fe (99.9+%, <10μm, Alfa Aesar) and iron sulfide (FeS, 99.99%, Alfa Aesar) in Fe+12.5 wt% S ($Fe_{80}S_{20}$), Fe + 23 wt% S ($Fe_{67}S_{33}$) compositions. The Fe-FeS compositions were ground in ethanol in a pestle and mortar for 1 hour then mixed dry for a short interval to homogenize any density settling during alcohol evaporation.

Pressure was generated using BX-90-type (Kantor et al. 2012) diamond anvil cells (DAC) with type 1 Boehler-Almax conical diamonds and seats, and Mao symmetric-type DACs with

Type 1 standard cut diamonds mounted on tungsten carbide of cubic-boron nitride (cBN) seats. Diamond culets ranged from 150-50 μm in diameter. Foils of $Fe_{80}S_{20}$ or $Fe_{67}S_{33}$ were produced by pressing the Fe–S starting powders between two ungasketed diamond anvils, then loaded between pellets of KCl or SiO_2. Sample chambers ranged from 180-25 μm in diameter and were drilled from pre-indented rhenium gaskets. Samples were dried at 100º C for 30 minutes prior to pressurization.

Angle dispersive X-ray diffraction (XRD) experiments were conducted at Argonne National Laboratory, Sector 13 ID-D, of the Advanced Photon Source. At Sector 13 ID-D, a 2.5 μm x 3.54 μm full width, half maximum (FWHM) monochromatic X-ray beam tuned to 37 or 42 keV was utilized, and diffracted X-rays were collected with a CdTe 1M Pilatus detector. Sample-to-detector geometries were calibrated using a LaB_6 NIST standard and a single crystal of enstatite was used for calibration of the rotational geometry of the X-ray beam and detector.

Double-sided laser heating and *in-situ* XRD collection took place at Sector 13 ID-D. Fiber lasers shaped with ~10 μm radius flat tops were aligned with the X-ray beam using the X-ray fluorescence of the sample pressure media or the gasket (Prakapenka et al., 2008). During heating, thermal emission from a 6 μm central region of the laser-heated spot was measured spectroradiometrically and fit to a gray body approximation (Heinz and Jeanloz, 1987). A 3% temperature correction was then applied to correct for axial gradients through the sample (Campbell et al., 2007; 2009). The laser power on each side of the sample was adjusted to maintain uniform double-sided heating and X-ray diffraction and temperature measurements were collected every ~200 K with 1s exposure times. Samples were typically quenched at high temperatures within 30-45 minutes of heating or after a phase transition and suitable grain growth was observed. Powder diffraction patterns were processed using Dioptas (Prescher and

Prakapenka, 2015) and CrysalisPro (Rigaku OD, 2018). Pressure was determined using the equation of state of hcp-Fe (Dewaele et al. 2006).

Upon quenching, X-ray diffraction maps of the heated spot were collected across a 100 μm^2 square region in 3 μm steps. Map locations showing high intensity, spotty diffraction patterns were chosen for multigrain single-crystal type X-ray diffraction collection approach, as these features indicate high-temperature induced crystallite growth. At chosen map locations, X-ray diffraction images were collected across ±17 to ±30º rotational scans in 0.25º–0.5º steps with 1– 4 s exposure times. The diffraction reflections were then mapped in the reciprocal space and target grains were identified and separated from reflections associated with the pressure media, iron, and diamond (Rigaku OD, 2018).

Target Fe-S lattices were then indexed, and the peak intensities were integrated and reduced using CrysalisPro (Rigaku OD, 2018). Absorption corrections and scaling factors were applied to the structure factors in CrysalisPro using the multi-scan method via the Scale3 Abspack program (Rigaku OD, 2018). The final structure factors and lattice geometries were then refined to known structure models (El-Boragy et al. 1970; Oryshchyn et al. 2011) using SHELXL2014/7 (Sheldrick 2015). Reflections showing anomalous calculated versus measured structure factors; likely due to overlap with diamond and other phases in the multigrain sample, resolution limitations, and volume of crystal illuminated by the X-ray beam, were omitted. Structure models were visualized using Vesta (Momma and Izumi 2011) during the refinement procedure.

3. RESULTS

3.1 Synthesis and identification of Fe_5S_2 to 200 GPa

Upon compression between 119(2) and 193(4) GPa and with heating to temperatures between 2400–3300 K, the diffraction patterns are characterized by recrystallized of hcp-Fe and diffuse streaks and sets of closely spaced reciprocal nodes suggestive of a complex atomic arrangement of the coexisting sulfide (Figure 1, S1). With sustained heating, large sulfide grain growth (3 – 6 μm) is observed (Figure 1). The diffraction angles for this synthesized sulfide phase are not compatible with the Fe_3P-type Fe_3S at these conditions (Kamada et al., 2014). Recrystallization of hcp-Fe with the sulfide crystallites at high temperatures was observed in all experiments using the $Fe_{80}S_{20}$ and $Fe_{67}S_{33}$ starting powders as evidenced by the spotty (100) and (101) hcp-Fe rings in Figure 1a. Fe recrystallization with this high-temperature Fe-sulfide establishes that the probed sample locations were in a Fe-saturated phase field (Figure 1a) and this sulfide phase is important to consider further in the context of Fe-rich planetary cores.

Upon temperature quenching in this pressure range, diffraction images were collected while rotating the DAC across a +/- 17–30º range (depending on the DAC configuration). Grains of a hexagonal lattice were identified in the reciprocal space with indexed parameters: a = 5.979(3) Å, c = 11.088(6) Å at 140(2) GPa and 3070(180) K (Figure 1b, Table 1). However, across the P-T explored, three polytypes were observed for this phase (Table 1). Each indexed grain exhibits an a axial length of ~ 6 Å, while 3 differing c axial lengths are observed: ~ 11, 26, and 73 Å. Diffraction mappings show that the polytypism is accompanied by diffuse scattering along the c direction suggesting positional disorder along this axis (Figure S1). Decreased diffuse scattering is observed after continued heating at peak temperatures in the KCl pressure media,

and grains with $a \sim 6$ Å, $c \sim 11$ Å were indexed (Figure 1b). This unit cell likely represents the most positionally ordered arrangement relevant at these high *P-T* conditions.

The crystal structure of the Fe-sulfide synthesized at 140(2) GPa and 3070(180) K was determined based on 159 observed reflections at these extreme conditions (Table 2). Assessment of the systematic absences for the reduced structure factors suggests a $P6_3cm$ space group, and structural solution and positional and displacement parameter refinement converged on an Fe_5S_2 compound adopting the Ni_5As_2 structure type (Table 2, 3; Figure 2) (Oryshchyn et al. 2011). The measured unit cell parameters for this polytype are compatible with 6 formula units per cell volume of Fe_5S_2. Furthermore, analogous polytypism due to stacking variations along the *c* direction have been observed in related transition metal binary phases such as Pb_5As_2 (Saini et al. 1964). The diffraction angles and intensities measured in this study cannot be modeled based on the tetragonal Fe_3S structure previously reported at these conditions (Kamada et al., 2012; Ozawa et al., 2013; Mori et al., 2017).

The Ni_5As_2 structure that Fe_5S_2 adopts is a slight modification of the Pb_5Sb_2 structure (El-Boragy et al. 1970), where the *M*6 site (*M* = metal) (Table 3) is split about its position given half occupancy, changing its Wyckoff site from 6c to 12d (Figure 2) (Oryshchyn et al. 2011). A significant improvement to the Fe_5S_2 refinement statistics was observed when incorporating the disordered Fe6 site, suggesting that the Ni_5As_2 structure model better describes the Fe_5S_2 structure factors (Table 2). Displacement parameters for the Fe_5S_2 structure model were refined as isotropic. Displacement parameters showing errors > 3$\boldsymbol{\sigma}$ were fixed to a value equal to the average displacement parameter value for Fe or S sites (Table 3). The isotropic displacement parameter for the disordered Fe site was also fixed at an average Fe_{Uiso} value (Table 3). The number of reflections collected at these extreme pressures limits the number of statistically

meaningful parameters to refine, and fixing displacement parameters to reasonable values precludes overinterpretation of the current dataset. The high isotropic displacement parameter observed on the Fe4 site may represent some vacancies on this site, but the dataset is again deficient to refine site occupancies (Table 3).

A CIF file for the final Fe_5S_2 structure model is provided in Appendix A1. Following previous descriptions of related M_5X_2 phases (e.g. Kjekshus et al. 1973; Oryshchyn et al. 2011), Fe_5S_2 can be viewed as an arrangement of 6 Fe sites and 3 S sites with the Fe1, Fe2, Fe4, and Fe6 sites in 13-fold coordination, the Fe3 and Fe5 sites in 12-fold coordination, and the S sites in 10-fold coordination (Figure 2c, Table 4). All sites are coordinated by both Fe and S sites.

Final R_1 values $\simeq$ 10% attest to the less-than ideal quality of the multigrain dataset as a possible result of the 1-2 megabar synthesis conditions and observed *c* axial disorder and stacking complexities in Fe_5S_2 (Table 2). Previous studies of isomorphic Ni_5As_2 and related Pb_5As_2 at ambient conditions have also reported similar quality of refinements despite obtaining significantly more reflections in the absence of a DAC (e.g. Saini et al. 1964; El-Boragy et al. 1970; Kjekshus et al. 1973). Notable challenges regarding the refinement of the Fe_5S_2 structure model at these extreme conditions are discussed here and compared with similar difficulties reported in previous characterizations of this structure type.

Thirteen violations of the $P6_3cm$ systematic absence condition: $l = 2n + 1$ for $(0kl)$, were flagged during the refinement of Fe_5S_2. The reflections associated with these systematic absence violations were examined in the raw diffraction images and show low, diffuse intensity. Discrepancy over the presence or absence of weak reflections with $(0kl)$, l=2n has been reported in previous investigations of Ni_5As_2 and Pb_5As_2 (e.g. Saini et al. 1964; El-Boragy et al. 1970; Kjekshus et al. 1973), suggesting that these studies also faced difficulties with space-group

determination. Observations of these low-intensity reflections could be a result of residual disorder along the *c* direction, and longer heating cycles may be required for the atoms to arrange into equilibrium positions. It is likewise possible that varying synthesis methods for Ni_5As_2 and Pb_5As_2 in previous ambient condition studies affected the *c* axial atomic arrangement. Ni_5As_2 and isomorphic Ni_5P_2 also exhibits a homogeneity range of ~71.25 – 72.7 atomic % As (Kjekshus et al. 1973; Litasov et al., 2019), and slight modifications of this structure based stoichiometric and stacking variations result in trigonal structures such as $Ni_{31}Si_{12}$ (Frank and Schubert 1971) and $(Fe, Ni)_8(Si, P)_3$ (perryite) (Okada et al. 1991). Attempts to refine the current Fe-sulfide phase with the $Ni_{31}Si_{12}$ or perryite structure models did not significantly improve the refinement statistics as the current high *P-T* dataset is too limited to resolve the intricacies that differentiate these structures. Based on the presence of disorder, polytypism, anisotropic vibrational motion, and nonstoichiometry in the related M_5X_2 phases, additional nuances to the Fe_5S_2 structure model may be developed in future studies; however, the identification and characterization of the Fe_5S_2 crystal structure determined here to 200 GPa is novel, and the observations and challenges reported in this study align with that of previous analyses of Ni_5As_2 and Pb_5Sb_2 that were not affected by the limitations associated with performing microdiffraction in a DAC at extreme conditions.

3.2 Other sulfides observed during heating to 200 GPa and comparison of their structures with Fe_5S_2

X-ray diffraction from seven heating cycles performed between 100 and 200 GPa and to 3300 K provide insight into the Fe-rich Fe-S phase relations at outer core pressures and to high temperatures. In each heating experiment, temperatures near melting were attained, and lattices

of Fe_5S_2 were indexed in the reciprocal space upon quenching. By further probing locations across the thermal gradient of the laser heated spots, additional Fe-sulfides were characterized, offering information on the lower temperature Fe-saturated sulfide crystal chemistries (Table 1, 2). These include Fe_3P-type Fe_3S (*I*-4, *Z* = 8), *C*23 Fe_2S (Co_2P-type, *Pnma*, *Z* = 4), and *C*37 Fe_2S (Co_2Si-type, *Pnma, Z*=4), in lower temperature regions at 119 GPa, 131 GPa, and 140 GPa, respectively (Figure 3; Table 1, 2).

Grains of tetragonal Fe_3S (*I*-4, *Z* = 8) (referred to herein as *I*-4 Fe_3S) were indexed with parameters: *a* = 8.094(3) Å, *c* = 3.990(2) Å at 119(2) GPa, and refined to the Fe_3P-type structure model (*I*-4, *Z* = 8) (referred to herein as *I*-4 Fe_3S), in agreement with previous studies (Fei et al. 2000; Seagle et al. 2006; Morard et al. 2007; Kamada et al. 2010; Kamada et al. 2012; Thompson et al. 2020) (Table 2, Figure 3a, Appendix A2). The structure can be viewed as containing 3 tetrahedrally coordinated Fe sites (Blanchard et al. 2008): one Fe-site is coordinated only by S atoms with an average bond length of 2.083(9) Å, another Fe site is coordinated by 3 S atoms and 1 Fe atom with an average bond length of 2.146(8) Å, and the third Fe site is coordinated by 2 S and 2 Fe atoms with an average bond length of 2.137(8) Å (Figure 3). The measured interatomic distances are comparable to reports on other transition metal M_3X structures (e.g. Aronnson 1955; Rundqvist 1979).

After heating at 131(2) GPa, grains of Fe_3S were not observed across the heated spot. Instead, orthorhombic lattices were also identified with parameters *a* = 4.869(2) Å, *b* = 3.256(2) Å, *c* = 6.139(2) Å, compatible with 4 formula units of Fe_2S. Structural solution and refinement indicate that the Fe_2S grains adopt the *C*23 structure (Co_2P type, *Pnma, Z* = 4) in agreement with previous structural analyses at lower pressures (Zurkowski et al. *in press*) (Table 2, Figure 3b, Appendix A3). The structure is composed of columns of FeS_4 tetrahedra and columns of FeS_5

288 square pyramids linked along edges in the *b* direction (Figure 3b). The average Fe–S bond
289 lengths are 2.213(8) Å and 2.011(2) Å in the square pyramids and tetrahedra, respectively. These
290 values are comparable with those observed in *C*23 Fe_2S at 90 GPa (Zurkowski et al. *in press*).
291 Upon temperature quenching at 140(2) GPa, orthorhombic grains were identified in the
292 sample chamber with *a* = 4.667(2) Å, 3.289(1) Å, 6.186(4) Å. This unit cell is similar to the *C*23
293 Fe_2S cell measured at 130 GPa, but it exhibits a 4 % contraction of the *a* axial length, a 1%
294 extension of the *b* and *c* axial lengths, and a 2% volume decrease. Structure solution and
295 refinement establishes that Fe_2S adopts the *C*37 structure (Co_2Si-type, *Pnma, Z*=4) (Table 2,
296 Figure 3c, Appendix A4). This result confirms the previously proposed *C*23–*C*37 transition in
297 Fe_2S at these conditions and presents a comparable volume change (Zurkowski et al., *in press*).
298 Inherent to the *C*23–*C*37 transition is coordination change from the 4-fold Fe1 coordination
299 polyhedra in the *C*23 structure to the 5-fold dipyramid polyhedra in the *C*37 structure (Figure 3b,
300 c). Comparing the *C*23 and *C*37 structure models determined at 130 and 140 GPa, respectively, a
301 10% contraction of the interatomic distance involved in the coordination change is observed
302 (Figure S2). The average Fe–S bond lengths measured in *C*37 Fe_2S are 2.196(2) Å and 2.165(3)
303 Å in the square pyramids and dipyramids, respectively. These values are comparable with those
304 observed in *C*23 Fe_2S in this study.
305 Comparison of the interatomic distances and coordination environments in the Fe-
306 sulfides observed in this study distinguishes Fe_5S_2 as particularly unique among them. Within an
307 interatomic distance of 2.7 Å (Table 4, Appendix A1-A4), *C*23 and *C*37 Fe_2S consist of Fe sites
308 coordinated only by S, while Fe_3S and Fe_5S_2 mark a drastic increase in Fe-Fe bonding with Fe
309 surrounded by up to 9 Fe sites in both structures. However, Fe_5S_2 exhibits Fe-Fe bond lengths up
310 to 25% shorter than that observed in Fe_3S at these pressures, further distinguishing the increased

311 iron-iron interactions in the novel Fe_5S_2 at Earth and planetary core pressures (Figure 2c, Table
312 4).
313
314 *3.3 Fe-rich sulfide phase relations at core-mantle boundary pressures*
315 The presented single-crystal derived structures of Fe_5S_2, Fe_3S, *C*23 Fe_2S and *C*37 Fe_2S
316 were then used to inform the changes in diffraction patterns collected during heating between
317 110 and 200 GPa and to ~3250 K (Figure 4). Beginning at 112 GPa, diffraction signal from *C*23
318 Fe_2S coexisting with Fe was first identified upon heating of the $Fe_{80}S_{20}$ starting material to
319 ~2000 K (Figure 4). With continued heating, peaks associated with tetragonal Fe_3S were
320 observed over a limited temperature range ($\lesssim$ 2400 K) until diffuse scattering signal and Bragg
321 reflections from Fe_5S_2 first appeared. Crystallization of the Fe_5S_2 grains with hcp-Fe occurred
322 with continued heating to 119(2) GPa and 2840(180) K (Figure 4).
323 Upon heating beginning at 120 GPa, *C*23 Fe_2S was observed coexisting with Fe to 122(1)
324 GPa and 2290(120) K, above which the onset of diffraction from the Fe_5S_2 phase was identified
325 and Fe_5S_2 crystallites formed coexisting with hcp-Fe to 131(2) GPa and 3050(140) K (Figure 4).
326 *I*-4 Fe_3S was not observed. With continued heating cycles between 133(1) GPa and 194(2) GPa
327 and up to 3250 K, *C*37 Fe_2S coexists with Fe at moderate temperatures and a reaction to form
328 Fe_5S_2 occurs at high temperatures (Figure 4). A pressure-induced *C*23–*C*37 Fe_2S transition is
329 therefore constrained between 125 and 135 GPa, in agreement with previous investigations of
330 Fe_2S (Zurkowski et al. *in press*).

4. DISCUSSION

4.1 Discrepancies among the current and previous studies

Transitional metal binary compounds with metal-to-nonmetal ratios ranging from 2.33–2.66 (~70–73 atm% metal) predominantly adopt complex trigonal or hexagonal structures with considerable metal-metal bonding (Chen and Whitmire 2018 and references therein). Our observations of the disorder, polytypism, and complex coordination environments inherent to Fe_5S_2 demonstrate that it aligns with this systematic characterization. Interestingly, this work elucidates that the Fe_5S_2 atomic arrangement is thermodynamically favored and expresses greater Fe-Fe interactions at the extreme conditions of Earth's outer core compared to that of *I*-4 Fe_3S.

These results are contrary to previous reports of Fe_3S stability on to high temperatures in Fe-rich systems to 250 GPa (Kamada et al. 2010; Kamada et al. 2012; Ozawa et al. 2013; Mori et al. 2017), but our observations may account for these discrepancies. First, interpretation of Fe_5S_2 in the integrated powder diffraction patterns is difficult due to the variation in diffraction signal obtained from the Fe_5S_2 polytypes and the low intensity scattering from the disordered sites during its formation (Figure S1, S3). Fe_5S_2 also forms large crystallites, limiting the orientations of the phase and rendering indexation of all diffraction angles for Fe_5S_2 quite challenging without rotating the sample (Figure 1a). The implementation of single-crystal X-ray diffraction techniques at high pressures was critical in the current study to accurately characterize the hexagonal unit cell geometry and complex structure of the Ni_5As_2-like Fe_5S_2 and to constrain the stability field of *I*-4 Fe_3S.

Several studies have also reported chemically analyzed Fe_3S grains in samples recovered from high temperatures in the 200–250 GPa range (Mori et al. 2017; Yokoo et al. 2019; Ozawa et al. 2013), but the difference in Fe content between Fe_3S and Fe_5S_2 may be as few as 3%. This

value is generally within 3σ uncertainty reported for chemical analyses of samples recovered from these extreme conditions, posing another challenge for distinguishing between the synthesis of Fe_3S and Fe_5S_2. Furthermore, based on characterizations of the isomorphic Ni_5As_2 and Ni_5P_2, these structures exhibit a homogeneity range with up to ~73 atm% metal (Kjekshus et al. 1973; Litasov et al., 2019). TEM analysis of a Fe–S sample recovered from 236 GPa and 2980 K reveals sulfide grains with on average ~73 atm% Fe (Ozawa et al. 2013); this value is within 0.3–1.25 atom % of the possible range of Fe_5S_2 stoichiometries and 2 atomic percent less than an Fe_3S composition. The results from previous chemical analyses of samples recovered from outer core pressures and high temperatures (Mori et al. 2017; Yokoo et al. 2019; Ozawa et al. 2013) therefore do not contradict the current results, and simply indicate previous misinterpretation of Fe_5S_2 as Fe_3S, based on EDS measurements alone, in the absence of single-crystal diffraction analysis.

4.2 Sulfur in Earth and Planetary cores

The stability of Fe_5S_2 and the phase relations observed in this study present novel constraints on the material properties of Fe-sulfides at conditions relevant to Earth's outer core, Venus' core, and exoplanetary cores of similar size and core-mass fraction (CMF). Namely, at pressures ≥120 GPa, Ni_5As_2-type Fe_5S_2, not tetragonal Fe_3S as previously believed, is the relevant Fe-rich sulfide. As Earth's outer core crystallizes over time, Fe_5S_2 will eventually crystallize over a large depth range up to the CMB. Tetragonal Fe_3S has been confirmed to 120 GPa (Figure 4) (Seagle et al. 2006; Morard et al. 2008; Thompson et al., 2020), constraining the $Fe_3S + Fe \rightarrow Fe_5S_2 + Fe$ transition to ~120 GPa. Rocky planetary bodies with sizes and CMFs like that of Venus (CMB = 114 GPa) (Aitta 2012) would likely crystallize Fe_3S at the CMB, but

Fe_5S_2 will be crystallizing over much of the core's depth. *C*37 Fe_2S is reported to be stable on the solidus above 306 GPa in Fe-rich systems (Tateno et al. 2019), suggesting a Fe_5S_2 + Fe → Fe_2S + Fe transition in the 200–300 GPa range. *C*37 Fe_2S remains the candidate Fe-rich sulfide at Earth's ICB, but for planets like Venus with a central pressure of 274 GPa (Aitta 2012), Fe_5S_2 may instead be the relevant Fe-rich sulfide, necessitating experimental determination of the Fe_5S_2→ Fe_2S + Fe decomposition *P*-*T* boundary. Furthermore, as Fe_5S_2 exhibits a complex crystalline arrangement with increased metal-metal bonding compared to Fe_2S and Fe_3S at core pressures, the significant depth over which Fe_5S_2 crystallizes in and Venus- to Earth-sized planetary cores may also contribute to higher conductivity signatures in these regions.

The stability of Fe_5S_2 coexisting with Fe between 120 and 200 GPa to to 3250 K also requires a change in melting behavior associated with the change in solidus phase from *I*-4 Fe_3S to Fe_5S_2 above 120 GPa. As Fe_5S_2 is observed to temperatures of ~3250 K, a kink in the Fe-sulfide solidus curve (Mori et al. 2017) is proposed to accommodate this (Figure 7). Further work examining melt signal will be helpful for accurately determining the shape of the solidus curve above 120 GPa, but the disorder observed in Fe_5S_2 may challenge the determination of melting that is commonly based on diffuse scattering appearing in the diffraction background. Further changes in melting relations occur as *C*37 Fe_2S becomes stable to melting temperatures above 306 GPa, and future experiments must investigate the change in melting temperatures associated with this transition at lower outer core conditions.

Terrestrial core chemistries are multicomponent; Si and Ni are also important core-alloying elements in planets such as Earth, drawing attention to the potential stability of the perryite $(Fe, Ni)_8(Si, P)_3$ structure in (Fe, Ni) – (Si, S)-rich cores. Perryite, observed in enstatite chondrites and aubrites, adopts a trigonal stacking variant of the Ni_5As_2-type structure (Wasson

and Wai, 1970; Okada et al. 1991), and iron phosphides tend to adopt analog structures to those observed in iron sulfides (i.e., Fei et al. 2000; Dera et al. 2008; Gu et al. 2014; Gu et al. 2016; Zurkowski et al., in press). Hence, Fe_5S_2 could potentially serve as a host for nickel and silicon in its perryite-like structure at Earth's outer core conditions. Furthermore, Si has recently been shown to dissolve into iron-sulfide phases and expand their stability field to higher pressure (Tao and Fei, 2021). The dissolution of silicon into Fe_5S_2 may expand its stability to higher pressures, making it potentially relevant at Earth's ICB conditions. If this is the case, the partitioning of Si and Ni between $(Fe, Ni)_5(S, Si)_2$ and (Fe, Ni, Si) and the density difference between the inner-core-crystallizing phase and remaining light-element-rich liquid will be crucial to investigations of the inner-core-density deficit and inner core seismic morphology.

5. CONCLUSIONS

To assess the phase stability of Fe-rich sulfides at Earth's outer core conditions, Fe-rich sulfide compositions were examined to 200 GPa and 3250 K using single-crystal and powder X-ray diffraction techniques in a laser-heated diamond anvil cell. At high temperatures between 120 and 200 GPa Fe_5S_2 is synthesized in the Ni_5As_2-type structure. The atomic arrangement of this hexagonal structure is characterized by positional disorder, complex coordination environments and significant Fe-Fe interactions. Additional polytypism and disorder associated with various stacking arrangements along the *c* direction are also observed. Along with Fe_5S_2, grains of *I*-4 Fe_3S, *C*23 Fe_2S, and *C*37 Fe_2S were also characterized. The stability of tetragonal Fe_3S in Fe-rich systems is constrained to below 120 GPa. *C*23 Fe_2S + Fe is observed at moderate temperatures to 130 GPa, and *C*37 Fe_2S + Fe is observed at moderate temperatures above 140 GPa. Between 120 and 200 GPa at the highest temperatures probed, Fe_5S_2 is stable coexisting

with Fe, therefore establishing that Fe_5S_2, not Fe_3S, is stable in Fe-rich systems at outer core pressures associated with Earth- and Venus-sized bodies. Fe_5S_2 crystallization can be expected over a extensive depth range in the cores of these planetary bodies.

Acknowledgments

Portions of this work were performed at GeoSoilEnviroCARS (The University of Chicago, Sector 13), Advanced Photon Source (APS), Argonne National Laboratory. GeoSoilEnviroCARS is supported by the National Science Foundation - Earth Sciences (EAR - 1634415). This research used resources of the Advanced Photon Source, a U.S. Department of Energy (DOE) Office of Science User Facility operated for the DOE Office of Science by Argonne National Laboratory under Contract No. DE-AC02-06CH11357. This material is based upon work supported by a National Science Foundation Graduate Research Fellowship to C.C.Z. This work was also supported by the National Science Foundation by grant EAR-1651017 to A.J.C.

6. TABLES

Table 1. Unit cell parameters of Fe_5S_2, Fe_3S, and Fe_2S measured upon quenching from high *P-T* synthesis in this study. Each cell was indexed in the reciprocal space, and the DAC opening, and number of reflections obtained for each lattice are listed. For select experiments, high-temperature synthesis was conducted without collecting X-ray diffraction data, and the synthesis conditions for these experiments are listed as "high T, not measured."

			Room temperature collection								Synthesis conditions	
Sample name	Starting material	medium	Phase	P GPa	*a* Å	*b* Å	*c* Å	V Å^3	DAC opening (°)	no. of reflections	*P* GPa	*T* K
C140_P2_map25	Fe80S20	KCl	Fe5S2	105(2)	6.020(4)		11.204(7)	351.6(5)	60	290	119(2)	2840(140)
C140_P2_map31	Fe80S20	KCl	Fe5S2	105(2)	6.050(2)		73.0(2)	2313(1)	60	134	119(2)	2840(140)
C140_P4_map10	Fe80S20	KCl	Fe5S2	118(1)	5.983(3)		11.078(6)	343.4(4)	60	489	140(2)	3070(180)
C140_P4_map14	Fe80S20	KCl	Fe5S2	118(1)	5.979(2)		11.084(4)	343.2(3)	60	379	140(2)	3070(180)
C140_P4_map14	Fe80S20	KCl	Fe5S2	118(1)	5.973(1)		11.094(2)	342.8(1)	60	276	140(2)	3070(180)
C129_P140_map71	Fe67S33	SiO2	Fe5S2	136.4(5)	5.957(4)		71.89(4)	2209(3)	34	84	159(2)	3230(150)
C129_P150_map9	Fe67S33	SiO2	Fe5S2	144.2(8)	5.939(3)		25.99(6)	794(2)	34	76	high T, not measured	
C129_P150_map9	Fe67S33	SiO2	Fe5S2	144.2(8)	5.923(1)		26.004(6)	789.9(3)	34	146	high T, not measured	
C137_P1_map25	Fe80S20	SiO2	Fe5S2	159(1)	5.890(3)		25.837(7)	776.2(5)	40	108	184(3)	3250(260)
C137_P1_map25	Fe80S20	SiO2	Fe5S2	159(1)	5.880(1)		25.789(3)	772.0(2)	40	108	184(3)	3250(260)
C137_P1_map25	Fe80S20	SiO2	Fe5S2	159(1)	5.876(2)		25.884(8)	774.0(4)	40	116	184(3)	3250(260)
C137_P1_map25	Fe80S20	SiO2	Fe5S2	159(1)	5.883(3)		25.85(1)	774.6(7)	40	126	184(3)	3250(260)
C137_P1	Fe80S20	SiO2	Fe5S2	159(1)	5.897(3)		25.90(1)	775.1(6)	40	116	184(3)	3250(260)
C137_P1	Fe80S20	SiO2	Fe5S2	159(1)	5.878(1)		25.784(3)	771.6(2)	40	149	184(3)	3250(260)
C137_P2_34	Fe80S20	SiO2	Fe5S2	179(1)	5.8400(7)		25.583(2)	755.7(1)	40	189	193(4)	3010(160)
C140_P1_map	Fe80S20	KCl	Fe3S	100(1)	8.156(3)		4.025(3)	267.8(3)	60	416	high T, not measured	
C140_P2_map25	Fe80S20	KCl	Fe3S	105(2)	8.094(3)		3.990(2)	261.4(2)	60	296	119(2)	2840(140)
C140_P3_map6	Fe80S20	KCl	*C*23Fe2S	111(1)	4.869(2)	3.256(2)	6.139(2)	97.3(1)	60	227	131(2)	3050(140)
C140_P4_map10	Fe80S20	KCl	*C*37 Fe2S	118(1)	4.677(2)	3.289(1)	6.186(4)	95.18(9)	60	188	140(2)	3070(180)

458 **Table 2.** Select experimental details for crystal structure synthesis and analysis of Fe_5S_2, Fe_3S,
459 and the Fe_2S polymorphs.

Phase	**Fe_5S_2**	**Fe_3S**	***C*23 Fe_2S**	***C*37 Fe_2S**
Sample Name	**C140_P4_map10**	**C140_P2_map25**	**C140_P3_map6**	**C140_P4_map10**
Synthesis				
Pressure (GPa)	140(2)	119(2)	131(2)	140(2)
Synthesis Temperature (K)	3070(180)	2840(140)	2050(140)	3070(180)
Symmetry	Hexagonal, *P*6(3)*cm*, Z=6	Tetragonal, *I*-4, Z=8	Orthorhombic, *Pnma*, *Z* = 4	Orthorhombic, *Pnma*, *Z* = 4
a (Å)	5.979(2)	8.094(3)	4.869(3)	4.677(2)
b (Å)			3.256(4)	3.289(1)
c (Å)	11.087(6)	3.990(2)	6.139(2)	6.186(4)
V (Å^3)	343.2(3)	226.4(2)	97.3(1)	95.18(9)
Reduction				
No. of measured, independent and observed [I > 2σ(I)] reflections	396, 309, 157	332, 314, 219	227, 208, 112	188, 158, 105
R_{int}, R_{sigma}	0.092, 0.062	0.053, 0.072	0.012, 0.016	0.009, 0.014
Refinement				
$R[F^2 > 2\sigma(F^2)]$, $wR(F^2)$, S	0.098, 0.255, 1.12	0.067, 0.164, 1.05	0.053, 0.149, 1.21	0.047, 0.139, 1.22
No. of reflections	156	219	112	105
No. of parameters	21	17	10	10
$\Delta\rho_{max}$, $\Delta\rho_{min}$ (e Å^{-3})	2.14, -2.18	1.92, -1.68	1.86, -2.02	1.91, -2.21

460
461
462
463
464

Table 3. Atomic coordinates of the Fe_5S_2 refinement model for the data collected at 140(2) GPa and quenched from 3070(180) K.

Wycoff site	ATOM	x	y	z	Uiso
2a	**Fe1**	0	0	0.963	0.021
	error			0.003	0.005
4b	**Fe2**	1/3	2/3	0.089	0.046
	error			0.003	0.005
6c	**Fe3**	0.259	0	0.126	0.021
	error	0.002		0.001	
6c	**Fe4**	0.613	0	0.222	0.021
	error	0.002		0.001	0.003
6c	**Fe5**	0.284	0	0.330	0.027
	error	0.002		0.001	0.003
12d	**Fe6***	0.651	0.056	0.426	0.021
	error	0.003	0.003	0.002	
2a	**S1**	0	0	0.220	0.026
	error			0.004	
4b	**S2**	1/3	2/3	0.299	0.026
	error			0.002	
6c	**S3**	0.673	0	0.030	0.026
	error	0.005		0.003	

*indicates half occupancy

Table 4. Selected interatomic distances for the Fe sites measured in Fe_5S_2 at 140 GPa. The "#" column indicates that number of the "bonded to" sites around the central atom.

Atom	bonded to	#	distance (Å)
Fe1	–Fe3	3	2.39(2)
	–Fe5	3	2.22(3)
	–Fe6	3	2.313(17)
	–S1	1	2.66(8)
	–S4	3	2.09(3)
Fe2	–Fe3	3	2.275(3)
	–Fe4	3	2.375(16)
	–Fe6	3	2.40(3)
	–S3	1	2.36(4)
	–S4	3	2.108(13)
Fe3	–Fe1	1	2.39(2)
	–Fe2	2	2.275(8)
	–Fe4	3	2.350(15)
	–Fe5	1	2.30(3)
	–Fe6	1	2.307(17)
	–S1	1	1.90(4)
	–S4	3	2.68(3)
Fe4	–Fe2	2	2.375(16)
	–Fe3	3	2.320(11)
	–Fe5	3	2.416(14)
	–Fe6	1	2.303(17)
	–S1	1	2.326(11)
	–S3	2	2.044(16)
	–S4	1	2.10(3)
Fe5	–Fe1	1	2.22(3)
	–Fe3	1	2.30(3)
	–Fe4	3	2.416(14)
	–Fe6	3	2.135(15)
	–S1	1	2.09(5)
	–S3	2	2.184(10)
	–S4	1	2.27(3)
Fe6	–Fe1	1	2.313(17)
	–Fe2	2	2.40(3)
	–Fe3	1	2.307(17)
	–Fe4	1	2.303(17)
	–Fe5	3	2.135(15)
	–S3	2	2.15(3)
	–S4	3	2.17(3)

Figures

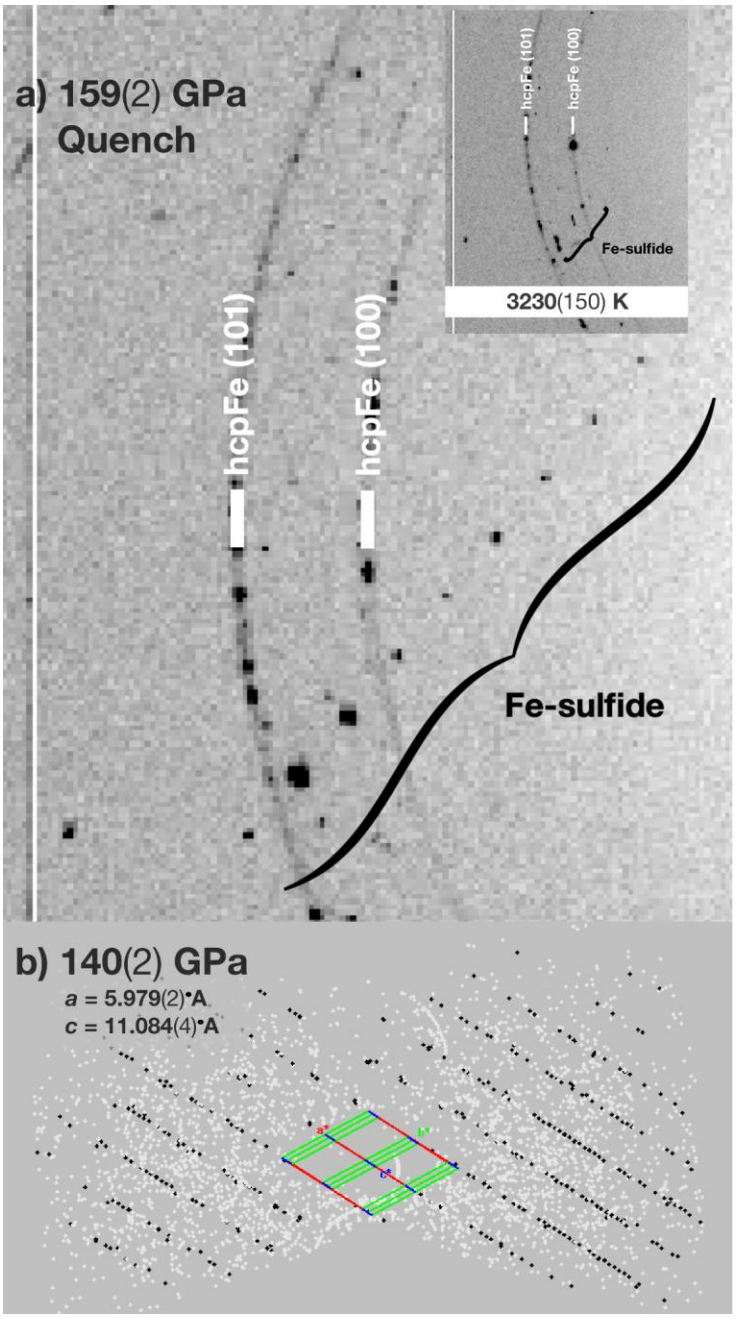

Figure 1. a) View of a crystallite of the high-temperature Fe_5S_2 coexisting with recrystallized hcp-Fe after synthesis at 159(2) GPa and 3230(130) K (inset). The spotty rings corresponding to the hcp-Fe (100) and (101) planes demonstrate that iron equilibrated at 159(2) GPa and 3230(130) K. b) View of the reciprocal space for reflections detected in an experiment on the $Fe_{80}S_{20}$ composition quenched from 140(2) GPa and 3070(140) K. The reciprocal lattice, colored in black, is associated with a Fe_5S_2 grain whose lattice parameters are provided in the top left.

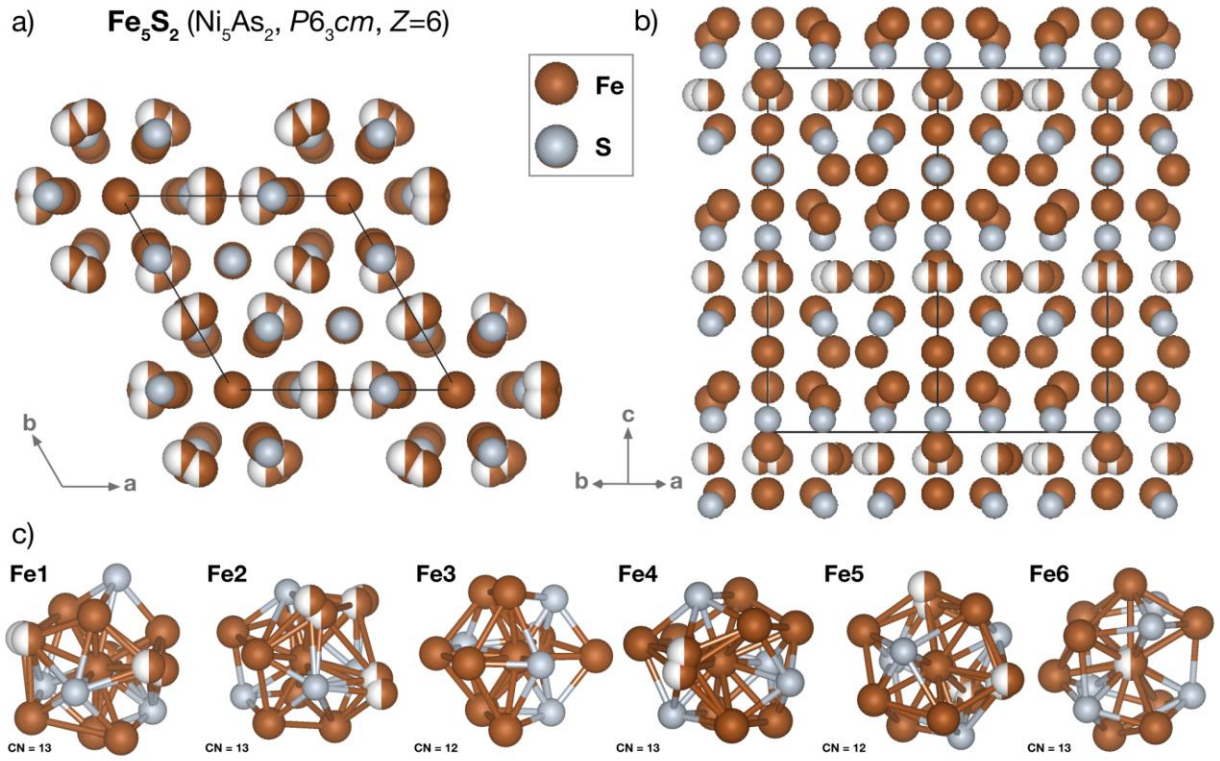

Figure 2. Crystal structure of Fe_5S_2 viewed along the a) *c* axis and the b) (100) plane. c) The Fe-coordination polyhedra observed in this atomic arrangement are provided. Fe1, Fe2, Fe4, and Fe6 are coordinated by 13 sites and Fe3 and Fe5 are coordinated by 12 sites. Each coordination polyhedron consists of Fe and S sites.

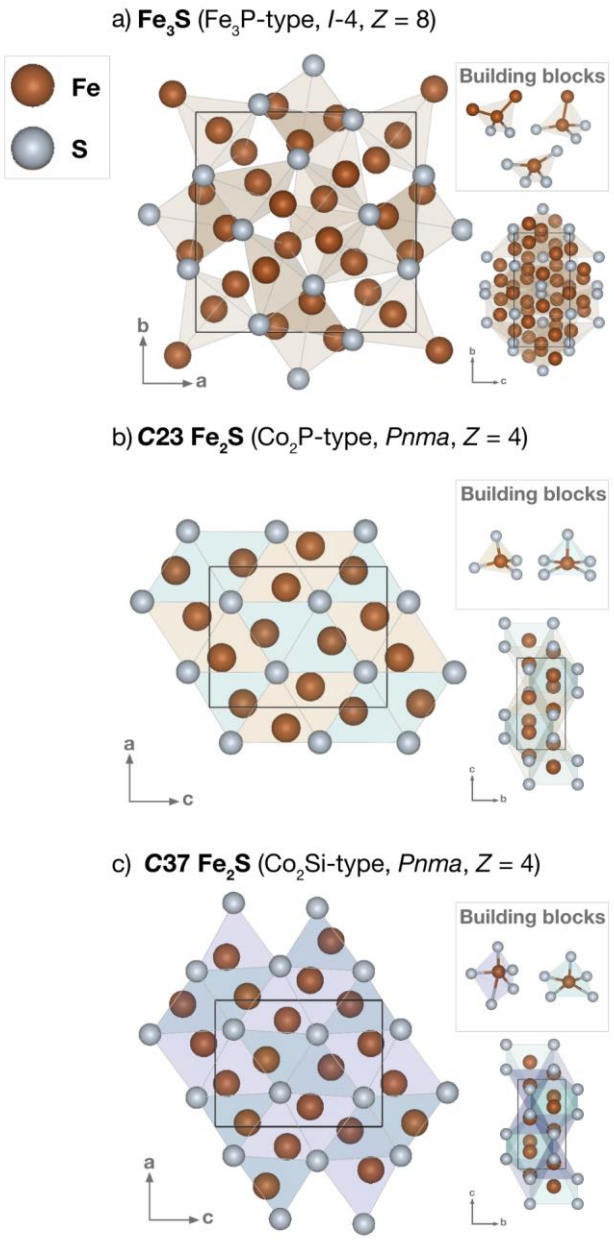

Figure 3. Crystal structures of Fe_3S and Fe_2S observed in this study. a) Fe_3S adopts the Fe_3P-type structure (*I*-4, *Z* = 8) that is composed of three tetrahedrally coordinated Fe-sites, each with increasing Fe–Fe bonding. b) The *C*23 Fe_2S structure (Co_2P-type, *Pnma*, *Z* = 4) is made up of columns of FeS_4 tetrahedra and columns of FeS_5 square pyramids linked along edges in the *b* direction. c) The *C*37 Fe_2S structure (Co_2Si-type, *Pnma*, *Z* = 4) has the same site symmetries as the *C*23 structure, but is marked by a shortened *a* axis and elongated *b* and *c* axes accompanied by the formation of a 5-fold dipyramid.

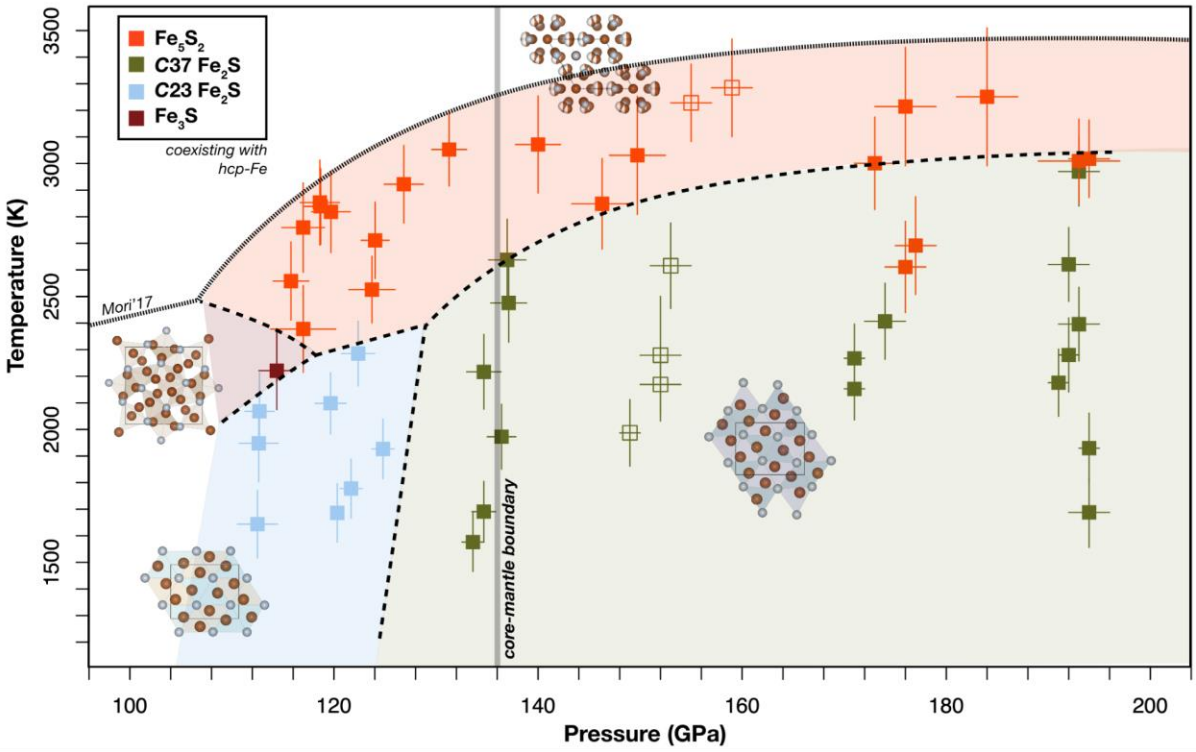

Figure 4. The single-crystal derived structures of Fe_5S_2, Fe_3S, and Fe_2S were then used to interpret the diffraction patterns collected during heating (Figure S3). At moderate temperatures, Fe_3S is observed below 120 GPa, *C*23 Fe_2S is observed below 130 GPa, and *C*37 Fe_2S is observed above 130 GPa. At high temperatures to 200 GPa, Fe_5S_2 is stable, and a kink in the Fe-S solidus curve (Mori et al., 2017) is presented to account for the change from Fe_3S to Fe_5S_2 melting in Fe-rich systems above ~120 GPa. The closed squares represent experiments conducted on the $Fe_{80}S_{20}$ starting material, and the open squares represent experiments conducted on the $Fe_{67}S_{33}$ starting material. Both show compatible results and iron recrystallization at high temperatures, indicating that Fe-rich regions of the $Fe_{67}S_{33}$ foils were probed.

8. SUPPLEMENTAL

Figure S1. Unwarped diffraction mappings of the (1*kl*), (0*kl*), and (-1*kl*) directions for an Fe_5S_2 crystallite exemplifying the diffuse scattering signal collected at 119(2) and 2840(180) K. The (1*kl*) and (-1*kl*) mappings also show the presence of a polytype with more closely spaced reflections oriented ~51º from the mapped crystallite.

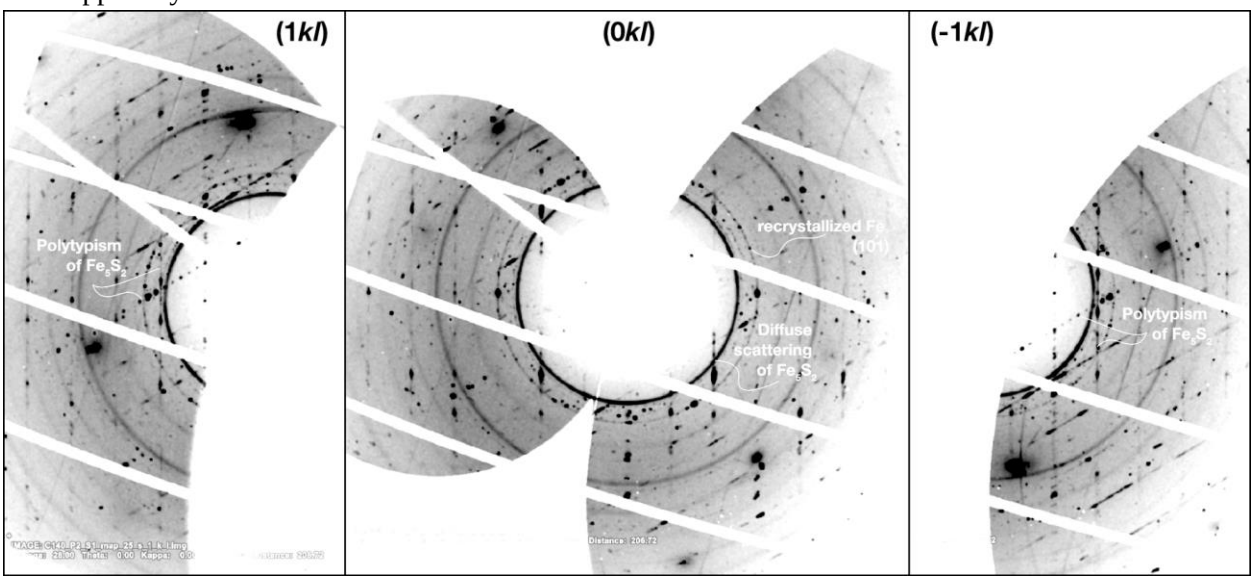

Figure S2. Comparison of the *C*23 and *C*37 Fe_2S structure models refined at 130 and 140 GPa, respectively. In the *C*23 Fe_2S structure, the next nearest sulfur site to the Fe1 tetrahedral site is at a 2.963(1) Å distance at 130 GPa (dotted line). A 10% contraction of this interatomic distance and a coordination change is observed in the formation of *C*37 Fe_2S at 140 GPa (right).

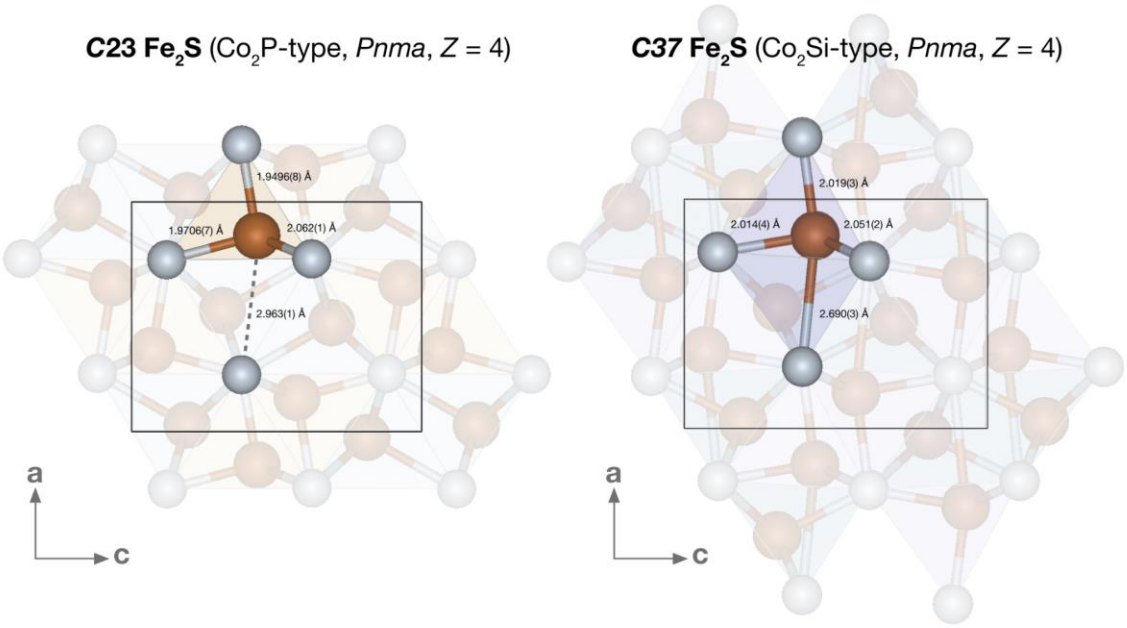

Figure S3. X-ray diffraction patterns collected upon heating in an $Fe_{80}S_{20}$ starting composition at a) 119(2) GPa and b)184(3) GPa. The miller indices for *C*23 Fe_2S (blue), Fe_3S (burgundy), and *C*37 Fe_2S (green) are provided, and the red "H" symbols represent the observations of the formation of Fe_5S_2. The growth of large crystallites, along with the disorder and polytypism of this phase make for challenging powder diffraction indexing, but the lattice parameters of Fe_5S_2 indexed in the reciprocal space after quenching from these high *P*-*T* conditions are provided.

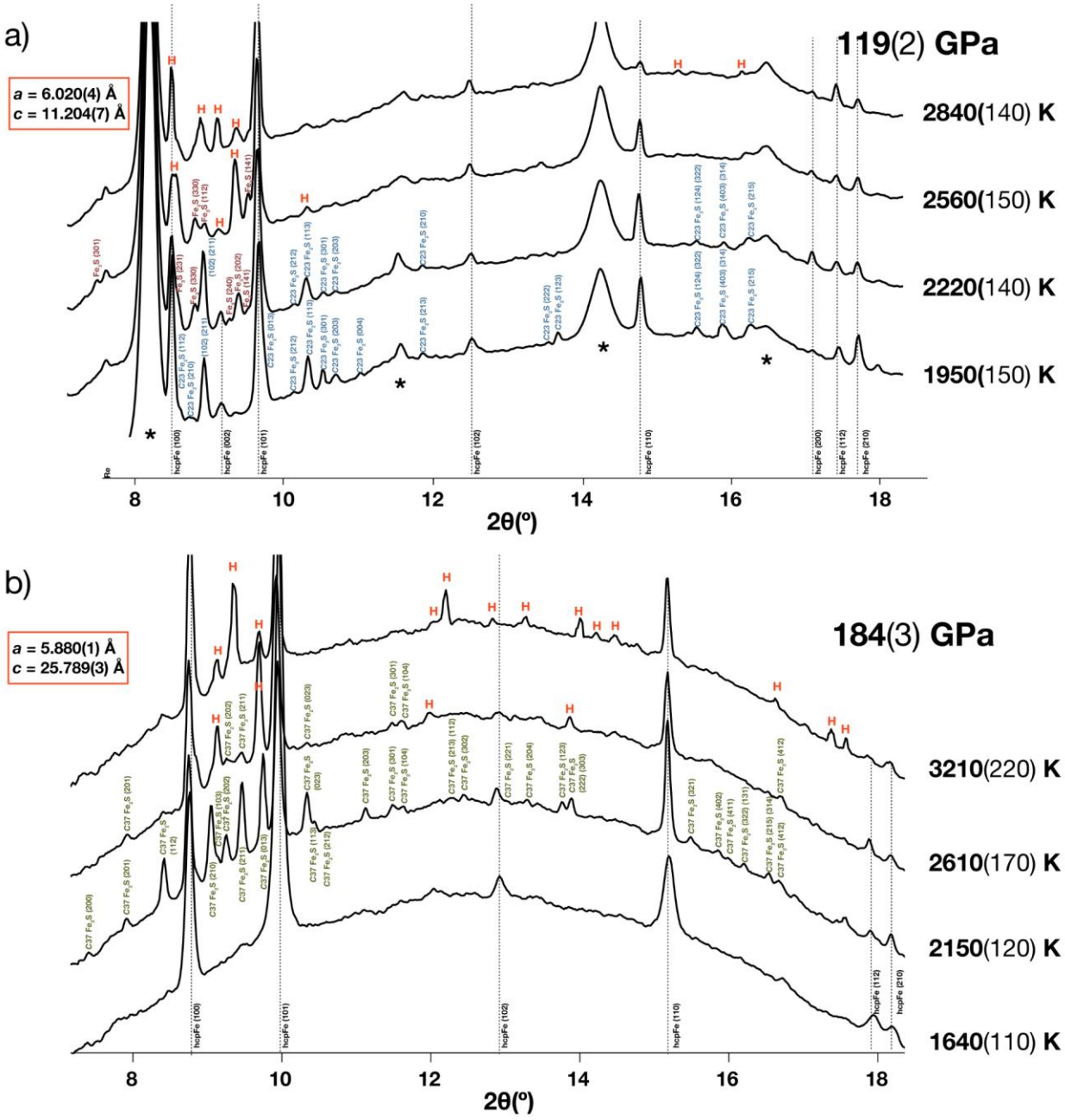

References

Anzellini, S., Dewaele, A., Mezouar, M., Loubeyre, P. and Morard, G., 2013. Melting of iron at Earth's inner core boundary based on fast X-ray diffraction. Science, 340, 464–466. https://doi.org/10.1126/science.1233514

Birch, F., 1952. Elasticity and constitution of the Earth's interior. J. Geophys. Res., 57, 227–286. https://doi.org/10.1029/JZ057i002p00227

Campbell, A.J., Seagle, C.T., Heinz, D. L., Shen, G., and Prakapenka, V.B., 2007. Partial melting in the iron-sulfur system at high pressure: A synchrotron X-ray diffraction study. Phys. Earth Planet. Inter., 162, 119–128. https://doi.org/10.1016/j.pepi.2007.04.001

Campbell, A.J., Danielson, L., Righter, K., Seagle, C.T., Wang, Y. and Prakapenka, V.B., 2009. High pressure effects on the iron–iron oxide and nickel–nickel oxide oxygen fugacity buffers. Earth Planet. Sci. Lett., 286, 556–564. https://doi.org/10.1016/j.epsl.2009.07.022

Chen, J.H. and Whitmire, K.H., 2018. A structural survey of the binary transition metal phosphides and arsenides of the d-block elements. Coord. Chem. Rev., 355, 271–327. https://doi.org/10.1016/j.ccr.2017.08.029

Dewaele, A., Loubeyre, P., Occelli, F., Mezouar, M., Dorogokupets, P.I. and Torrent, M., 2006. Quasihydrostatic equation of state of iron above 2 Mbar. Phys. Rev., 97, 215504. https://doi.org/10.1103/PhysRevLett.97.215504

Dziewonski, A.M. and Anderson, D.L., 1981. Preliminary reference Earth model. Phys. Earth Planet. Inter., 25, 297–356. https://doi.org/10.1016/0031-9201(81)90046-7

El-Boragy, M., Bhan, S. and Schubert, K., 1970. Kristallstruktur von Pd_5Sb_2 und Ni_5As_2 und einigen varianten. J. less-common met, 22, 445–458. https://doi.org/10.1016/0022-5088(70)90132-3

Evans, H.T., 1970. Lunar troilite: crystallography. Science, 167, 621–623. https://doi.org/10.1126/science.167.3918.621

Fearn, D.R. and Loper, D.E., 1981. Compositional convection and stratification of Earth's core. Nature, 289, 393–394. https://doi.org/10.1038/289393a0

Fei, Y., Prewitt, C.T., Mao, H.K. and Bertka, C.M, 1995. Structure and density of FeS at high pressure and high temperature and the internal structure of Mars. Science, 268, 1892–1894. https://doi.org/10.1126/science.268.5219.1892

Fei, Y., Bertka, C.M. and Finger, L.W., 1997. High-pressure iron-sulfur compound, Fe_3S_2, and melting relations in the Fe–FeS system. Science, 275, 1621–1623. https://doi.org/10.1126/science.275.5306.1621

Fei, Y., Li, J., Bertka, C.M. and Prewitt, C.T., 2000. Structure type and bulk modulus of Fe_3S, a new iron-sulfur compound. Am. Mineral., 85, 1830–1833. https://doi.org/10.2138/am-2000-11-1229

Fei, Y., Ricolleau, A., Frank, M., Mibe, K., Shen, G. and Prakapenka, V., 2007. Toward an internally consistent pressure scale. Proc. Natl. Acad. Sci. U.S.A., 104, 9182–9186. https://doi.org/10.1073/pnas.0609013104

Frank, K. and Schubert, K., 1971. Kristallstruktur von $Ni_{31}Si_{12}$. Acta crystallogr., B Struct.

crystallogr. cryst. chem., 27, 916–920. https://doi.org/10.1107/S0567740871003261
Heinz, D.L., and Jeanloz, R., 1987. Measurement of the melting curve of $Mg_{0.9}Fe_{0.1}SiO_3$ at lower mantle conditions and its geophysical implications. J. Geophys. Res., 92, 437–444. https://doi.org/10.1029/JB092iB11p11437
Irving, J.C., Cottaar, S. and Lekić, V., 2018. Seismically determined elastic parameters for Earth's outer core. Sci. Adv., 4, 2538. https://doi.org/10.1126/sciadv.aar2538
Jephcoat, A. and Olson, P., 1987. Is the inner core of the Earth pure iron? Nature, 325, 332–335. https://doi.org/10.1038/325332a0
Jones, J.H. and Drake, M.J., 1983. Experimental investigations of trace element fractionation in iron meteorites, II: The influence of sulfur. Geochim. Cosmochim. Acta., 47, 1199–1209. https://doi.org/10.1016/0016-7037(83)90062-5
Kamada, S., Terasaki, H., Ohtani, E., Sakai, T., Kikegawa, T., Ohishi, Y., Hirao, N., Sata, N. and Kondo, T., 2010. Phase relationships of the Fe–FeS system in conditions up to the Earth's outer core. Earth Planet. Sci. Lett., 294, 94–100. https://doi.org/10.1016/j.epsl.2010.03.011
Kamada, S., Ohtani, E., Terasaki, H., Sakai, T., Miyahara, M., Ohishi, Y. and Hirao, N., 2012. Melting relationships in the Fe–Fe_3S system up to the outer core conditions. Earth Planet. Sci. Lett., 359, 26–33. https://doi.org/10.1016/j.epsl.2012.09.038
Kamada, S., Ohtani, E., Terasaki, H., Sakai, T., Takahashi, S., Hirao, N. and Ohishi, Y., 2014. Equation of state of Fe_3S at room temperature up to 2 megabars. Phys. Earth Planet. Inter., 228, 106-113. https://doi.org/10.1016/j.pepi.2013.11.001
Kantor, I., Prakapenka, V., Kantor, A., Dera, P., Kurnosov, A., Sinogeikin, S., Dubrovinskaia, N. and Dubrovinsky, L., 2012. BX90: A new diamond anvil cell design for X-ray diffraction and optical measurements. Rev. Sci. Instrum., 83, 125102. https://doi.org/10.1063/1.4768541
King, H. and Prewitt, C.T., 1982. High-pressure and high-temperature polymorphism of iron sulfide (FeS). Acta crystallogr., B Struct. crystallogr. cryst. chem., 8, 1877–1887. https://doi.org/10.1107/S0567740882007523
Kjekshus, A., Skaug, K.E., Hebrew, C., Van Buren, C.T., Klæboe, P. and Swahn, C.G., 1973. On the crystal structure of Ni_5As_2. Acta Chem. Scand., 27, 582–588.
Kruijer, T.S., Touboul, M., Fischer-Gödde, M., Bermingham, K.R., Walker, R.J. and Kleine, T., 2014. Protracted core formation and rapid accretion of protoplanets. Science, 344, 1150–1154. https://doi.org/10.1126/science.1251766
Kuwayama, Y., Morard, G., Nakajima, Y., Hirose, K., Baron, A.Q., Kawaguchi, S.I., Tsuchiya, T., Ishikawa, D., Hirao, N. and Ohishi, Y., 2020. Equation of state of liquid iron under extreme conditions. Phys. Rev., 124, .165701. https://doi.org/10.1103/PhysRevLett.124.165701
Litasov, K.D., Shatskiy, A.F., Minin, D.A., Kuper, K.E. and Ohfuji, H., 2019. The Ni–Ni_2P phase diagram at 6 GPa with implication to meteorites and super-reduced terrestrial rocks. High Press. Res., 39, 561–578. https://doi.org/10.1080/08957959.2019.1672677
Maaref, S., Madar, R., Chaudouet, P., Fruchart, R., Senateur, J.P., Averbuch-Pouchot, M.T.,

669 Bacmann, M., Durif, A. and Wolfers, P., 1983. Etude de la structure et des conditions de
670 stabilite d'un nouvel arseniure de fer: $Fe_{12}As_5$. Mater. Res. Bull., 18, 473-480.
671 https://doi.org/10.1016/0025-5408(83)90139-3
672 Malvin, D.J., Wang, D. and Wasson, J.T., 1984. Chemical classification of iron meteorites—X.
673 Multielement studies of 43 irons, resolution of group IIIE from IIIAB, and evaluation of
674 Cu as a taxonomic parameter. Geochim. Cosmochim. Acta., 48, 785–804.
675 https://doi.org/10.1016/0016-7037(84)90101-7
676 Masters, G. and Gubbins, D., 2003. On the resolution of density within the Earth. Phys. Earth
677 Planet. Inter., 140, 159–167. https://doi.org/10.1016/j.pepi.2003.07.008
678 McDonough, W.F. and Sun, S.S., 1995. The composition of the Earth. Chem. Geol., 120,
679 223–253. https://doi.org/10.1016/0009-2541(94)00140-4
680 McDonough, W.F., 2003. Compositional model for the Earth's core. In The Mantle and Core
681 (Ed. R. W. Carlson), Vol. 2 Treatise on Geochemistry (Exec. Eds. H. D. Holland and K.
682 K. Turekian), 547–568.
683 Momma, K. and Izumi, F., 2011. VESTA 3 for three-dimensional visualization of crystal,
684 volumetric and morphology data. J. Appl. Crystallogr., 44, 1272–1276.
685 https://doi.org/10.1107/S0021889811038970
686 Morard, G., Andrault, D., Guignot, N., Sanloup, C., Mezouar, M., Petitgirard, S. and Fiquet, G.,
687 2008. In situ determination of Fe–Fe_3S phase diagram and liquid structural properties up
688 to 65 GPa. Earth Planet. Sci. Lett., 620–626. https://doi.org/10.1016/j.epsl.2008.05.028
689 Mori, Y., Ozawa, H., Hirose, K., Sinmyo, R., Tateno, S., Morard, G. and Ohishi, Y., 2017.
690 Melting experiments on Fe–Fe_3S system to 254 GPa. Earth Planet. Sci. Lett.,
691 464 135–141. https://doi.org/10.1016/j.epsl.2017.02.021
692 Murthy, V.R. and Hall, H.T., 1970. The chemical composition of the earth's core: Possibility of
693 sulfur in the core. Phys. Earth Planet. Inter., 2, 276–282.
694 https://doi.org/10.1016/0031-9201(70)90014-2
695 Nimmo, F., 2015. Thermal and compositional evolution of the core. In Core Dynamics (Ed.
696 Peter Olsen). Vol. 8 Treatise on Geophysics, (Exec. Eds. G. Schubert), 217–241.
697 Okada, A., Kobayashi, K., Ito, T. and Sakurai, T., 1991. Structure of synthetic perryite,
698 $(Ni, Fe)_8(Si, P)_3$. Acta Crystallogr. C Struct. Chem., 47, 1358–1361.
699 https://doi.org/10.1107/S0108270191000483
700 Oryshchyn, S., Babizhetskyy, V., Zhak, O., Stoyko, S., Guérin, R., and Simon, A., 2011. Crystal
701 structure of HT-Ni_5P_2 and reinvestigation of isotypic Ni_5As_2. Intermetallics, 19,
702 1041–1046. https://doi.org/10.1016/j.intermet.2011.03.013
703 Ozawa, H., Hirose, K., Suzuki, T., Ohishi, Y. and Hirao, N., 2013. Decomposition of Fe_3S
704 above 250 GPa. Geophys. Res. Lett., 40, 4845–4849. https://doi.org/10.1002/grl.50946
705 Prakapenka, V.B., Kubo, A., Kuznetsov, A.Laskin, A., Shkurikhin, O., Dera, P., Rivers, M. L.
706 and Sutton, S.R., 2008. Advanced flat top laser heating system for high pressure research
707 at GSECARS: application to the melting behavior of germanium. High Press. Res., 28,
708 225–235. https://doi.org/10.1080/08957950802050718

709 Prescher, C., and Prakapenka, V.B., 2015. DIOPTAS: a program for reduction of two
710 dimensional X-ray diffraction and data exploration. High Press. Res., 35(3), 223– 230.
711 https://doi.org/10.1080/08957959.2015.1059835
712 Ricard, Y., Šrámek, O. and Dubuffet, F., 2009. A multi-phase model of runaway core–mantle
713 segregation in planetary embryos. Earth Planet. Sci. Lett., 284, 144–150.
714 https://doi.org/10.1016/j.epsl.2009.04.021
715 Rigaku Oxford Diffraction, 2018. CrysAlisPRO software system, ver. 1.171.39.44a Rigaku
716 Corporation, Oxford, U.K.
717 Ringwood, A.E., 1966. The chemical composition and origin of the Earth. Advances in earth
718 science, 65, 287.
719 Rubie, D.C., Frost, D.J., Mann, U., Asahara, Y., Nimmo, F., Tsuno, K., Kegler, P., Holzheid, A.
720 and Palme, H., 2011. Heterogeneous accretion, composition and core–mantle
721 differentiation of the Earth. Earth Planet. Sci. Lett., 301, 31–42.
722 https://doi.org/10.1016/j.epsl.2010.11.030
723 Rundqvist, S., 1960. The structures of Co_2P, Ru_2P and related phases. Acta Chem.
724 Scand., 14, 1961–1979.
725 Rundqvist, S. and Jellinek, F., 1959. The structures of Ni_6Si_2B, Fe_2P and some related phases.
726 Acta Chem. Scand., 13, 425–432.
727 Saini, G.S., Calvert, L.D., and Taylor, J.B., 1964. Compounds of the type M_5X_2: Pd_5As_2, Ni_5Si_2,
728 and Ni_5P_2. Can. J. Chem., 42, 1511–1517. https://doi.org/10.1139/v64-233
729 Scott, E.R. and Wasson, J.T., 1975. Classification and properties of iron meteorites. Rev.
730 Geophys., 13, 527–546. https://doi.org/10.1029/RG013i004p00527
731 Seagle, C.T., Campbell, A.J., Heinz, D.L., Shen, G. and Prakapenka, V.B., 2006. Thermal
732 equation of state of Fe_3S and implications for sulfur in Earth's core. J. Geophys. Res. Solid
733 Earth, 111. https://doi.org/10.1029/2005JB004091
734 Shannon, M.C. and Agee, C.B., 1996. High pressure constraints on percolative core formation.
735 Geophys. Res. Lett., 23, 2717–2720. https://doi.org/10.1029/96GL02817
736 Sheldrick, G.M., 2015. Crystal structure refinement with SHELXL. Acta Crystallogr. C Struct.
737 Chem., 71, 3–8. https://doi.org/10.1107/S2053229614024218
738 Stevenson, D.J., 1981. Models of the Earth's core. Science, 214, 611–619.
739 https://doi.org/10.1126/science.214.4521.611
740 Stevenson, D.J., 1988. Fluid dynamics of core formation. In Topical Conference Origin of the
741 Earth (Vol. 681, p. 87).
742 Tateno, S., Ozawa, H., Hirose, K., Suzuki, T., I-Kawaguchi, S., and Hirao, N., 2019. Fe_2S: the
743 most Fe-rich iron sulfide at the Earth’s inner core pressures. Geophys. Res. Lett., 46,
744 11,944–11,949. https://doi.org/10.1029/2019GL085248
745 Wasson, J.T. and Wai, C.M., 1970. Composition of the metal, schreibersite and perryite of
746 enstatite achondrites and the origin of enstatite chondrites and achondrites. Geochim.
747 Cosmochim. Acta, *34*, 169-184. https://doi.org/10.1016/0016-7037(70)90004-9
748 Yoshino, T., Walter, M.J. and Katsura, T., 2003. Core formation in planetesimals triggered by

permeable flow. Nature, 422, 154–157. https://doi.org/10.1038/nature01459
Yokoo, S., Hirose, K., Sinmyo, R. and Tagawa, S., 2019. Melting experiments on liquidus phase relations in the Fe-S-O ternary system under core pressures. Geophys. Rev. Lett., 46, 5137–5145. https://doi.org/10.1029/2019GL082277
Zurkowski, C.C., Lavina, B., Chariton, S., Tkachev, S., Prakapenka V.B. and Campbell A.J., *in press*. The crystal structure of Fe_2S at 90 GPa based on single-crystal X-ray diffraction techniques. American Mineralogist, https://doi.org/10.2138/am-2022-7973
Zurkowski, C. C., Lavina, B., Brauser, N. M., Davis, A. H., Chariton, S., Tkachev, S., Greenberg, E., Prakapenka, V. B., and Campbell, A. J., *in press.* Pressure-induced *C*23-*C*37 transition and compression behavior of orthorhombic Fe_2S to Earth's core pressures and high temperatures. https://doi.org/10.2138/am-2022-8187